Nature Communications

https://doi.org/10.1038/s41467-026-69962-4

Article in Press

Photoelectrocatalytic-microbial biohybrid for succinic acid synthesis

Received: 20 February 2025

Accepted: 13 February 2026

Cite this article as: Feng, T., Zhou, X., Zhang, Y. *et al.* Photoelectrocatalytic-microbial biohybrid for succinic acid synthesis. *Nat Commun* (2026). https://doi.org/10.1038/s41467-026-69962-4

Tianhang Feng, Xue Zhou, Yingjie Zhang & Zhonghai Zhang

Photoelectrocatalytic-microbial biohybrid for succinic acid synthesis

Tianhang Feng[1,#], Xue Zhou[1,#,*], Yingjie Zhang[1], Zhonghai Zhang[1,*]

[1] School of Chemistry and Molecular Engineering, East China Normal University, Shanghai 200241, China

[#] These authors contributed equally.

*Corresponding authors: Zhonghai Zhang (zhzhang@chem.ecnu.edu.cn); Xue Zhou (xzhou@chem.ecnu.edu.cn)

Abstract

Succinic acid is an important platform chemical traditionally produced via energy-intensive and environmentally unfriendly processes. *Actinobacillus succinogenes* offers a sustainable biosynthetic route, yet its productivity is constrained by limited intracellular electron transfer. Here, we develop a photoelectrocatalytic–microbial biohybrid system to overcome these metabolic bottlenecks. Adaptive laboratory evolution using gold nanoparticles establishes an enhanced charge-transfer pathway in *Actinobacillus succinogenes*, which is subsequently immobilized on a layer-by-layer NiO@PAA@NHS (NiO nanosheets coated with hydrogel of poly acrylic acid (PAA) grafted with N-Hydroxysuccinimide (NHS)) photoelectrode to construct a NiO@PAA@NHS/Au@ *Actinobacillus succinogenes* biohybrid. Under simulated solar illumination at −0.3 V vs. RHE, the system delivers a photocurrent density of 1.9 mA cm^{-2}, a CO_2 conversion efficiency of 67%, and a succinic acid production rate of 1.41 ± 0.04 g L^{-1} h^{-1} cm^{-2}. This work demonstrates an effective strategy for coupling solar energy with microbial metabolism for scalable, carbon-neutral chemical production.

Introduction

Succinic acid, alternatively referred to as amber acid or 1,4-butanedioic acid, is a promising raw material to produce 1,4-butanediol, γ-butyrolactone, tetrahydrofuran, 2-pyrrolidinone, and polybutylene succinate [1,2]. This versatile compound is widely applied across industries, including chemical synthesis, food flavoring and preservation, pharmaceutical manufacturing, and the development of biodegradable plastics [3,4]. Therefore, it is listed as one of the twelve high-value chemicals by the U.S. Department of Energy [5]. The market for succinic acid is anticipated to experience a compound annual growth rate of 10.6%, and it is projected that by the year 2026, the market will surpass the value of 200 million US dollars [6]. Currently, most of commercially available succinic acid is produced by chemical process, in which liquefied petroleum gas or maleic anhydride is used as a starting material [7,8]. However, the process poses several environmental and health concerns due to the release of greenhouse gases and pollutants, and the by-products generated in this process are toxic and require careful disposal [9]. Therefore, there is a growing interest in developing more sustainable and environmentally friendly alternatives to the current chemical production methods of succinic acid.

Recent analysis has showed that bacterial fermentative production of succinic acid from renewable resources can be more cost-effective than the petroleum-based processes [10-12]. Many different microorganisms have been screened and studied for succinic acid production [13-15]. Among them, *Actinobacillus succinogenes* (*A. succinogenes*), a naturally succinic acid-producing strains isolated from bovine rumen, is one of the most intensively investigated bacterium for succinic acid

production [16]. The *A. succinogenes* has a natural capacity to convert both pentose and hexose sugars into succinic acid as an intermediate of the tricarboxylic acid (TCA) cycle [17]. Upon the absorption of the substrate glucose by the bacteria, it is converted into phosphoenolpyruvate (PEP), marking the beginning of the metabolic divergence into two distinct pathways [18,19]. One pathway is dedicated to the production of the desired product, succinic acid, and is primarily governed by the enzyme phosphoenolpyruvate carboxykinase (Pepck). Under the catalysis of PEPCK and with the aid of coenzymes such as NADH, CO_2 is incorporated into the metabolic pathway. PEP undergoes a series of enzymatic transformations, initially forming oxaloacetate, which is then reduced to malate through the action of malate dehydrogenase utilizing NADH. Subsequently, malate is converted to fumarate by fumarase, and finally, fumarate is transformed into succinic acid, the target product, in a reaction catalyzed by fumarate reductase. The other metabolic route, dominated by pyruvate kinase (PK), is responsible for the synthesis of by-products such as formic acid, acetic acid, and ethanol. This metabolic flexibility allows the bacteria to adapt to varying environmental conditions and substrate availabilities, optimizing the overall efficiency of succinic acid production within the PEC-bacterial biohybrid system. This metabolic pathway ingeniously incorporates CO_2 [20-22], rendering it an optimal candidate for transforming lignocellulosic sugars and CO_2 into bioproducts from sustainable feedstocks, and providing an additional advantage of contributing to the carbon peaking and carbon neutrality goals [23-26]. However, the inherent metabolic processes of microorganisms in the context of fermentation-based chemical synthesis impose constraints on the potential for increased product yields. Presently, two strategies have

been posited to surmount these limitations and to augment production metrics. The first strategy encompasses genetic engineering, leveraging targeted modifications to refine and optimize metabolic routes [27,28]. However, compared to commonly industrial microorganisms, the repertoire of genetic modification techniques for *A. succinogenes* is rather confined, which hinders the rate of strain improvement through genetic engineering. The alternative paradigm introduces the assembly of biohybrids, which entails the amalgamation of nanomaterials with bacterial systems to supply the microorganisms with surplus electrons and energy, consequently elevating production levels [29-31]. Consequently, in response to the growing demand for sustainable and environmentally friendly production methods, the engineering of biohybrids emerges as an innovative and exceptionally prospective pathway for enhancing succinic acid yields. While, this approach needs to address the critical requirements for sustainable energy input, efficient charge transfer, and intracellular electron transport, which are essential for enhancing succinic acid yields.

The photoelectrocatalytic-bacterial (PEC-bacterial) biohybrid system is a good candidate to harnesses sustainable solar energy and to drive the production of succinic acid from CO_2 and renewable resources. This system integrates photoelectrode with *A. succinogenes*, where the photoelectrode generates electrons upon illumination, and these electrons are transferred to the bacteria, facilitating the assimilation of CO_2 into succinic acid. As the most active bacteria at the biotic-abiotic interface are those directly connected to the photoelectrode, and that close microbial-electrode interactions can promote electron transport and CO_2 reduction efficiency [32,33]. Therefore, the effective integration of the photoelectrode with the bacteria is the prerequisites for efficient

charge transfer in the PEC-bacterial system. We draw inspiration from several innovative studies, for examples, Zhang [34] has designed 3D printed hierarchical column array electrodes that significantly boost bacterial loading efficiency. Additionally, Erwin Reisner [35] has proposed an IO-ITO electrode with a hydrophilic surface and porous structure, which facilitates bacterial affinity. Liu [36] has also contributed to the field with an in-situ chemical reaction-mediated covalent localization strategy of bacteria, where thiolated bacteria bind to poly(disulfide)s-abundant mucin located at various tissue interfaces.

Herein, the photoelectrode is designed with a typical p-type semiconductor of NiO nanosheets, which is coated with hydrogel of poly acrylic acid (PAA) grafted with N-Hydroxysuccinimide (NHS) (NiO@PAA@NHS). Hydrogel is a highly water-containing, three-dimensional network-structured material with excellent biocompatibility and ability to load a range of biologically active substances, such as bacteria, which not only have good adhesion to the bacteria, but also promote bacterial colonization and activity over a long period of time [37,38]. Furthermore, to ensure efficient extracellular and intracellular electron transport, the gold nanoparticles (Au NPs) is incubated into bacteria through an adaptive laboratory evolution (ALE) strategy, pioneered by Prof. Peidong Yang [39], to form a conductive bridge that allows electrons generated extracellularly to be transported across the bacterial membrane and into the metabolic pathways of the bacteria. Moreover, the Au-ALE process can optimize the bacteria's electroactivity, enhancing their ability to acquire and transfer electrons, which in turn improves interfacial charge transport while maintaining bacterial vitality. [40]. Therefore, the PEC-bacterial biohybrid of

NiO@PAA@NHS/Au@*A. succinogenes* provides necessary metabolic energy to boost succinic acid production, and reach a high succinic acid yield rate of 1.41 ± 0.04 g L^{-1} h^{-1} cm^{-2} (0.012 ± 0.0003 mol mol L^{-1} h^{-1} cm^{-2}) at one atmospheric pressure saturated with CO_2 under illumination of solar light. This PEC-bacterial biohybrid is expected to be applied in large-scale, low-cost succinic acid production, providing another direction for CO_2 reduction, and sustainably producing high-value long-chain hydrocarbons. This innovative approach leverages solar energy and biohybrid technology to produce high-value chemicals in a sustainable and environmentally friendly manner.

Results

Construction of the PEC-Bacterial Biohybrid System

The PEC-bacterial biohybrid reactor, as schematically illustrated in Fig. 1a, is designed with a NiO@PAA@NHS/Au@*A. succinogenes* biohybrid photoelectrode to leverage the metabolic capabilities of *A. succinogenes* for the synthesis of succinic acid from CO_2 under solar light illumination. Fig. 1b illustrates the interaction between the PAA@NHS hydrogel and the A. succinogenes cell membrane. The ester groups (C=O) on the hydrogel surface interact with the amino groups (N-H) of membrane proteins through possible amide linkage formation, promoting robust bacterial adhesion on the photoelectrode surface. However, the current spectroscopic evidence only indicates interfacial coupling rather than definitive covalent bond formation.

Notably, these bacteria have been adapted after Au-adaptive laboratory evolution (ALE) process, introducing Au NPs near the inner cell membrane. This strategic introduction of Au NPs establishes an efficient charge transfer pathway, enhancing the charge transfer efficiency and, consequently, increasing the yield of PEC production of succinic acid. This innovative approach highlights the potential of combining biocompatible materials with nanoscale engineering to optimize bio-photoelectrochemical systems.

Characterization of Bacterial Modification and Surface Immobilization

The Au NPs were introduced into *A. succinogenes* with an ALE strategy. As illustrated in Fig. 2a, this strategy enabled the bacteria to adapt to and tolerate the presence of these Au NPs. This process is essential for creating a biohybrid system where the bacteria can utilize the Au NPs for enhanced electron transfer. In the ALE process, *A. succinogenes* were initially exposed to a low concentration of Au ions, allowing the bacteria to encounter the Au ions without causing immediate toxicity. The Au ions were taken up by the bacteria, possibly through active transport mechanisms or simple diffusion [41]. Once inside the cells, the Au ions are reduced to Au NPs by reductive substances present in the bacterial cells, such as NADH or other biomolecules with reducing properties [42-44]. As the bacteria are exposed to increasing concentrations of Au ions over time, they develop mechanisms to tolerate and manage the presence of these Au NPs. The Au-ALE allows the bacteria not only to tolerate but also to thrive in the presence of Au NPs, thus significantly enhancing their survival rates.

Fig. 2b displays a thin-sectioned transition electron microscopy (TEM) image of wild *A. succinogenes*, where it can be observed that the morphology is intact and spherical. As shown in Fig. 2c, the ALE of *A. succinogenes* with Au ions have resulted in the bacteria embedding Au NPs within their cellular structure, particularly near the inner wall of the bacterial cell membrane. The size distribution of Au NPs in bacteria is shown in Supplementary Fig. 1, with an average particle size of approximately 38 nm. The high-angle annular dark-field scanning transmission electron microscopy (HAADF-STEM) image in Fig. 2d reveals distinct bright spots, which, according to this characterization method, indicate a higher atomic number of an element. The brightness of the spots corresponds to the presence of elements with higher atomic numbers, and in this case, it further demonstrates the presence of Au NPs within the bacterial cells, located near the inner wall of the cell membrane. The corresponding energy-dispersive X-ray spectroscopy (EDS) mapping image in Fig. 2e for Au@*A. succinogenes* also confirms the successful entry of Au NPs into the bacterial cells. The EDS data shows a higher concentration of Au near the cell membrane, suggesting that the Au NPs were not only internalized by the bacteria but also accumulated near the cell membrane, as evidenced by the intense EDS signal for Au in that region. This membrane-associated localization of Au NPs can be attributed to their intracellular formation mechanism. During the ALE process, *A. succinogenes* gradually adapted to increasing concentrations of $HAuCl_4$, reducing Au^{3+} to Au^0 likely using intracellular reductants such as NADH and NADH-dependent reductases. Since many of these reductases are enriched at or near the inner membrane, the nucleation of Au^0

preferentially occurs in that region, resulting in the accumulation of Au NPs adjacent to the membrane. Although Fig. 2e shows the overall Au distribution, this proximity to the membrane is further supported by HAADF-STEM and EDS mapping. Such spatial positioning is essential for the Au NPs to serve as intracellular conduits for electron transfer, bridging photoelectrode-derived electrons with bacterial metabolic pathways without disrupting cellular viability.

Despite the presence of these Au NPs, we have observed that the bacteria continue to divide (Supplementary Fig. 2). Moreover, the uniform distribution of Au NPs within each bacterium further substantiates the successful complexation of the Au NPs and their excellent biocompatibility. Furthermore, we compared the viability of *A. succinogenes* cultured directly in a high-concentration Au ion solution (2 μM) versus those cultured using a stepwise acclimation approach (0.5 μM, 1 μM, 1.5 μM, and 2 μM) with flow cytometry (Supplementary Fig. 3). As shown in Fig. 2f, the apoptotic analysis revealed that 73.1% of the 100,000 bacteria treated directly with 2 μM $HAuCl_4$ underwent apoptosis. In contrast, when bacteria were adapted to 2 μM $HAuCl_4$, the survival rate surged to 89.1%. This significant difference demonstrates that the ALE approach is an effective way to introduce high concentrations of Au NPs within bacterial cells, which is crucial for enhancing charge transfer efficiency. All these micromorphological and elemental evidences provide compelling evidence of the intracellular localization of Au NPs, highlighting their potential role in facilitating electron transfer processes within the bacteria and potentially enhancing the overall efficiency of the PEC-bacterial biohybrid system.

The Au-ALE *A. succinogenes* bacteria are adsorbed onto the surface of photoelectrodes, which are prepared by coating a PAA@NHS hydrogel on NiO nanosheets (Fig. 2g). We performed FTIR spectroscopy to analyze the interfacial chemical environment (Supplementary Fig. 4). The free *A. succinogenes* spectrum shows distinct amide I (1627 cm^{-1}) and amide II (1533 cm^{-1}) bands [45]. After immobilization on NiO@PAA@NHS, new features emerge at 1685 cm^{-1} and 1625 cm^{-1} with significant attenuation of the amide II signal. This behavior suggests enhanced hydrogen bonding and possible amide-linkage interactions between bacterial surface proteins and the NHS-activated hydrogel layer [46]. The weakened amide II band is partly due to spectral overlap with the C=O stretching of the hydrogel ($\approx$1710 cm^{-1}) and the broad O-H/N-H bending envelope (1550-1650 cm^{-1}), indicating that these shifts reflect interfacial coupling rather than definitive covalent bond formation. Additionally, the band at 1043 cm^{-1} is attributed to C–O–C stretching vibrations of polysaccharides present on the bacterial cell wall or C–O stretching in polyacrylic acid (PAA) [47]. After incubating the bacteria-with NiO@PAA@NHS, NiO@PAA, and bare NiO electrodes in 0.1 M PBS solution for 30 min, CLSM analysis (Supplementary Fig. 5) revealed negligible bacterial detachment from the NiO@PAA@NHS electrode, whereas NiO@PAA and bare NiO controls showed stronger fluorescence signals corresponding to higher bacterial release. It is likely that the NHS-activated hydrogel layer could improve interfacial adhesion and biofilm stability.

The NiO nanosheets, synthesized via a hydrothermal method on nickel foam, exhibit a distinct lamellar structure with a fine, fluffy nanostructure as observed in the SEM image (Supplementary

Fig. 6). High-resolution TEM (HR-TEM) analysis reveals an interplanar spacing of 0.23 nm (Supplementary Fig. 7), corresponding to the (200) plane of NiO, confirmed by the XRD pattern (Supplementary Fig. 8).

The formation of the NiO@PAA@NHS sample was characterized using FTIR, Raman spectroscopy, and X-ray photoelectron spectroscopy (XPS). The FTIR analysis (Supplementary Fig. 9) shows peaks at 1710 cm^{-1}, 1423 cm^{-1}, and 1270 cm^{-1}, corresponding to the stretching vibration of the C=O bond, the scissor bending vibration of $-CH_2$, and the stretching vibration of C-N, respectively [48]. A new Raman peak (Supplementary Fig. 10) after encapsulating PAA@NHS can be assigned to C-H asymmetric stretching of PAA@NHS. The XPS data indicate a new N 1s peak and variation of O 1s peaks, evidencing the formation of the NiO@PAA@NHS material (Supplementary Fig. 11). The nanosheet structures are well-preserved after the PAA@NHS hydrogel coating, maintaining a predominantly rounded and smooth morphology (Supplementary Fig. 12). A TEM image further confirms the wrapping of PAA/NHS around the surface of the NiO nanosheets (Supplementary Fig. 13), and the crystal structure of NiO remains unchanged after the PAA@NHS coating, as shown by the XRD pattern (Supplementary Fig. 8). The elemental distribution on NiO@PAA@NHS is revealed by a HAADF-STEM image and corresponding EDS elemental mapping images (Supplementary Fig. 14), showing a uniform distribution of Ni, N, and O elements, with the nitrogen originating from the NHS component within the PAA@NHS hydrogel. Collectively, these results confirm the successful construction of the NiO@PAA@NHS photoelectrode.

After the successful fabrication of the NiO@PAA@NHS electrode, the *A. succinogenes* after the Au-ALE were adsorbed onto its surface. SEM analysis, as depicted in Fig. 2h and Fig. 2i, conducts a comparative assessment of bacterial cell counts and clearly illustrated a pronounced increase in bacterial colonization on the NiO@PAA@NHS photoelectrode surface. This increase indicates a marked enhancement in bacterial adhesion attributable to the presence of the PAA@NHS hydrogel layer. A quantitative summary of *A. succinogenes* bacteria is presented in Fig. 2j, showing an average bacterial count of $0.16\times10^6/mm^2$ on pristine NiO. In contrast, this count significantly rose to $2.6\times10^6/mm^2$ on the NiO@PAA@NHS surface. Such a substantial enhancement in bacterial adhesion highlights the critical role of surface functionalization in augmenting bacterial adhesion and metabolic activity within the PEC-bacterial biohybrid system. This surface modification is pivotal for creating a conducive environment for bacterial attachment and activity, thereby enhancing the overall performance of the biohybrid system.

Photoelectrocatalytic Performance of the Biohybrid System

The PEC activity of NiO@PAA@NHS/Au@*A. succinogenes* biohybrid was evaluated by linear sweep voltammetry (LSV) in an Ar- or CO_2-saturated electrolyte, in the dark or under illumination of simulated solar light (AM 1.5 G, 100 mW cm^{-2}). As depicted in Fig. 3a, in the Ar-saturated electrolyte, the NiO@PAA@NHS/Au@*A. succinogenes* biohybrid exhibited a weak photocurrent response. However, in the CO_2-saturated electrolyte, the current densities both in dark and under

illumination were significantly enhanced, indicating effective CO_2 reduction involvement in succinic acid production. The succinic acid yields were compared under CO_2 and Ar atmospheres with or without the addition of $Mg_2(OH)_2CO_3$. As a pH neutralizer, the $Mg_2(OH)_2CO_3$ also served as an additional carbon source during the reaction process. Therefore, when Ar was introduced without the addition of basic magnesium carbonate, *A. succinogenes* essentially produced no succinic acid (Supplementary Fig. 15). Furthermore, the current density on the NiO@PAA@NHS/Au@*A. succinogenes* biohybrid under illumination was much higher than that in the dark, suggesting more effective CO_2 reduction and a higher succinic acid yield in the PEC model than that in the electrocatalytic (EC) model. These observations underscore the system's capacity for CO_2 reduction and its efficient harnessing of photogenerated electrons, thereby enhancing succinic acid production.

The succinic acid yield rate of the NiO@PAA@NHS/Au@*A. succinogenes* biohybrid was evaluated under various operational models, revealing significant differences in performance. As presented in Fig. 3b, the PEC model (PEC-biohybrid) demonstrated the highest yield rate of 1.41±0.04 g L^{-1} h^{-1} cm^{-2} (0.012 ± 0.0003 mol mol L^{-1} h^{-1} cm^{-2}), showcasing its superior efficiency in succinic acid production. This outcome underscores the effectiveness of integrating light-based energy input to enhance bacterial metabolism and succinic acid generation. The EC model (EC-biohybrid) followed with a yield rate of 0.75±0.03 g L^{-1} h^{-1} cm^{-2}, while the photocatalytic model (PC-biohybrid) exhibited a rate around 0.58±0.06 g L^{-1} h^{-1} cm^{-2}. In contrast, the biohybrid under dark and open circuit conditions had the lowest yield

rate of 0.21±0.04 g L^{-1} h^{-1} cm^{-2}. These results suggest that external energy input, particularly through the PEC model, can substantially increase the rate of succinic acid production by *A. succinogenes*, highlighting the potential of this approach in bioprocess optimization and sustainable chemical production.

Fig. 3c provides a comparative analysis of the succinic acid yield rate across four biohybrid systems, including NiO@PAA@NHS/Au@*A. succinogenes*, NiO@PAA/Au@*A. succinogenes*, NiO/Au@*A. succinogenes*, and Au@*A. succinogenes*. The NiO@PAA@NHS/Au@*A. succinogenes* biohybrid system reaches the highest yield rate. The NiO@PAA/Au@*A. succinogenes* system also performs well, with a yield rate of 0.98±0.06 g L^{-1} h^{-1} cm^{-1}. In contrast, the NiO/Au@*A. succinogenes,* and the Au@*A. succinogenes*, which lack the additional components, show lower yield rates of just 0.47±0.03 g L^{-1} h^{-1} cm^{-1} and 0.21±0.02 g L^{-1} h^{-1} cm^{-1} respectively. Furthermore, the CO_2 conversion efficiency (Supplementary Fig. 16) and glucose conversion rate (Supplementary Fig. 17) were systematically analyzed across different systems. The NiO@PAA@NHS/Au@*A. succinogenes* biohybrid system demonstrated superior performance, achieving a remarkable 67% CO_2 conversion rate along with a glucose conversion yield of 0.78 $g/g_{glucose}$.These results underscore the importance of the biohybrid composition in maximizing succinic acid yield, with the NiO@PAA@NHS/Au@*A. succinogenes* system demonstrating the most promising results due to the contribution of Au NPs acting as an efficient charge transfer bridge and the hydrogel's effective adhesion to bacteria.

The photocurrent densities at different applied potentials of NiO@PAA@NHS/Au@*A.*

succinogenes biohybrid were compared and are presented in Fig. 3d. The biohybrid shows stable photocurrent performance, and the photocurrent density increases with more negative potentials, indicating efficient charge separation and transport at the PEC-bacterial model. In order to further screen the appropriate potential for succinic acid production, we comprehensively compared the succinic acid yield rate at different potentials. As shown in Fig. 3e, the NiO@PAA@NHS/Au@*A. succinogenes* biohybrid system reaches the highest succinic acid yield rate at -0.3 V (vs RHE), which can be attributed to a balance between electron supply and the metabolic demands of the bacteria. At -0.2 V (vs RHE), the photocurrent density is lower, suggesting that the electron supply to the biohybrid system is insufficient to meet the bacteria's needs for succinic acid production (Supplementary Fig. 18). This could be due to less efficient charge separation or a lower driving force for electron transfer at this potential. With increasingly negative potentials (-0.2 to -0.5 V vs RHE), the photocurrent density and H_2 evolution on the bare NiO@PAA@NHS photocathode both rose markedly (Supplementary Fig. 19). However, the highest succinic acid yield occurred at -0.3 V, indicating that excessive bias promotes H_2 generation rather than electron transfer to the bacteria for CO_2 fixation [49]. These results suggest that hydrogen evolution and transmembrane electron uptake are competitive processes, and that -0.3 V represents an optimal potential where interfacial charge transfer and microbial metabolism are effectively balanced.

In addition to succinic acid, other byproducts such as acetic acid, formic acid, and pyruvic acid were also measured in the biohybrid system. As presented in Fig. 3f, the yield rate of succinic acid is the fastest, indicating that it is the predominant product under the

given conditions, and it accounts for 57.18% of the total yield. To further analyze possible gaseous products, gas chromatography (GC) was performed to quantify H_2 and CO generated during the reaction. As shown in Supplementary Fig. 20, trace amounts of CO (~425.7 nmol after 3 h) and small amounts of H_2 (~144 μmol after 8 h) were detected. The calculated Faradaic efficiencies were 48.3% for the hydrogen evolution reaction (HER) and only 0.38% for CO formation from CO_2 reduction, confirming that gaseous CO_2RR products are negligible and that the majority of photogenerated electrons are utilized for microbial succinate synthesis rather than abiotic gas formation.

The long-term stability of the PEC-biohybrid system for succinic acid generation was evaluated to monitor the photocurrent (Supplementary Fig. 18) and cyclic PEC reactions (Supplementary Fig. 21). The photocurrent changes were negligible when the biohybrid system was operated at -0.3 V vs RH1E over a period of 10 hours, indicating a stable transfer of photoelectrons from the electrode to the bacteria. In addition, succinic acid yield was assessed over five consecutive cyclic reactions. There is a gradual decrease in succinic acid production after 5 days, which can be attributed to minor degradation of both the electrode materials and bacterial viability under prolonged PEC conditions.

Maintaining a consistent output is essential for the viability and efficiency of industrial production processes. Therefore, the continuous production of succinic acid by a biohybrid system under conditions that simulate day and night cycles, alternating between PEC and EC modes, was investigated. As shown in Fig. 3g, the simulation of a light–dark cycle of 12 hours

effectively mirrors the biohybrid system's capability to produce succinic acid for 5 days, highlighting the system's potential for sustained industrial application. It should be noted that the "superior efficiency" claim refers specifically to the higher succinic acid productivity achieved under PEC conditions (during the light phase), whereas EC conditions alone exhibit a relatively lower production rate. Nevertheless, alternating between PEC and EC modes is crucial to maintaining continuous and stable succinic acid production over extended periods.

Furthermore, to evaluate the biocompatibility of the biohybrid system, confocal laser scanning microscope (CLSM) images were taken before and after the PEC reaction (Supplementary Fig. 22). *A. succinogenes* was stained with the BBcellProbe N01™/PI fluorescent probe. The BBcellProbe N01™ can emit bright green fluorescence upon excitation due to its ability to penetrate the cell membrane of living bacteria. In contrast, PI can only stain dead bacteria, showing red fluorescence after excitation [50]. Compared to *A. succinogenes* before the reaction, after an extended reaction period, there was a significant increase in green fluorescence intensity, and a slight enhancement in the red fluorescence signal. This suggests that the bacteria were able to rapidly multiply within the system and that there was a natural generational turnover occurring. Additionally, a colony-forming unit (CFU) assay was conducted to assess bacterial viability (Supplementary Fig. 23). There was an increase in the bacterial count after the long-term reaction. Collectively, these findings further suggest that the *A. succinogenes* in the biohybrid system possesses robust self-repairing and self-replicating capabilities, indicating that the bacteria remain viable and active before and after the reaction, which is crucial for sustained functionality in

industrial applications.

The succinic acid yield rates in a PEC-biohybrid system were compared with various other biohybrid systems and bacterial strains under different reaction conditions (Supplementary Table 1). As shown in Fig. 3h, the biohybrid system operating in PEC mode demonstrated the highest succinic acid production rate among the systems tested, which is a testament to its superior efficiency. The PEC-biohybrid system's superior succinic acid yield rate, high biocompatibility, and long-term stability position it as a leading candidate for industrial-scale production and commercialization of this essential chemical.

During the succinic acid biosynthesis, synergistic catalysis between glucose and CO_2 is essential. The carbon origin distribution in succinate was precisely mapped through comprehensive ^{1}H and ^{13}C nuclear magnetic resonance (NMR) spectroscopic analysis. In the ^{1}H NMR spectrum (Supplementary Fig. 24a), the methylene proton peak appears at 2.34 ppm. Following $^{13}CO_2$ labeling, this signal remains unchanged. However, when labeled with $^{13}C_6H_{12}O_6$, the peak splits into a doublet, demonstrating that ^{13}C from glucose is incorporated into the succinic acid carbon skeleton through metabolic processes, inducing complex coupling (^{13}C-^{13}C coupling). For the ^{13}C-NMR analysis (Supplementary Fig. 24b), the carboxyl carbon (-COOH) resonates at 181 ppm, and its signal intensity increases significantly after $^{13}CO_2$ labeling, confirming that CO_2 fixation directly contributes to the carboxyl carbon. And the methylene carbon (-CH_2-) appears at 32 ppm, and both the methylene and carboxyl carbon signals show notable enhancement upon $^{13}C_6H_{12}O_6$ labeling. This indicates that the glucose carbon skeleton, via glycolysis/TCA cycle

metabolism, generates the methylene group and partially contributes to the carboxyl carbons of succinic acid. This dual-labeling NMR analysis provides clear evidence for the distinct biosynthetic origins of succinic acid's carbon backbone.

Mechanistic Insights into Enhanced Succinic Acid Production

Fig. 4a presents a schematic overview of succinic acid biosynthesis in the NiO@PAA@NHS/Au@*A. succinogenes* biohybrid, emphasizing glucose assimilation and redox modulation along the C4 metabolic pathway under photoelectrocatalytic conditions. In this system, electronic interactions at the biohybrid interface modulate intracellular redox states, thereby favoring succinate formation. Based on the additional electrochemical and control experiments, we suggest that direct electron transfer (DET) across the Au-mediated electrode-bacteria interface serves as the primary pathway, whereas H_2-mediated electron transfer makes a minor contribution under conditions study. Cyclic voltammetry (CV) analysis (Supplementary Fig. 25a) revealed that wild-type *A. succinogenes* exhibited intrinsically weak electroactivity, while Au-adapted cells showed pronounced redox peaks centered at approximately +0.15 V (vs RHE). The current density nearly doubled from ~0.45 mA cm^{-2} to ~0.85 mA cm^{-2}. In contrast, the CV profile of the cell-free supernatant was mostly featureless, ruling out contributions from soluble mediators or residual Au ions (Supplementary Fig. 25b). These results suggest that the Au nanoparticles formed near the inner membrane act as conductive nanoscale bridges, facilitating charge exchange between the photoelectrode and intracellular redox partners. The precise route of electron transport across the bacterial

membrane, however, requires further elucidation.

Although a minor indirect pathway may coexist, its contribution is small. Umol amounts of H_2 generated at the photocathode surface can be oxidized by membrane-bound hydrogenases and introduced into the bacterial redox network; however, the addition of external H_2 caused only a marginal increase in succinic acid production (Supplementary Fig. 26), confirming that the H_2-mediated route contributes minimally compared with the dominant DET process.

Fluorescence lifetime measurements (Fig. 4b) showed that Au@*A. succinogenes* exhibited a lifetime of 1.89 ns, representing a 45% reduction relative to the control, demonstrating that the incorporation of Au nanoparticles substantially accelerates intracellular electron transfer and charge separation.

To gain a deeper understanding of the internal metabolism of *A. succinogenes*, the relative ATP level and NADH/NAD^+ ratios were compared among three groups: *A. succinogenes*, NiO@PAA@NHS/*A. succinogenes*, and NiO@PAA@NHS/Au@*A. succinogenes*. As depicted in Fig. 4c, the ATP content in *A. succinogenes* increased by 21% upon biofilm formation with NiO@PAA@NHS, and this increase was even more pronounced, reaching 107%, in the NiO@PAA@NHS/Au@*A. succinogenes* system. This substantial boost in ATP is crucial for enhancing biochemical synthesis processes. Additionally, the NADH/NAD^+ ratio showed a 32% increase in the NiO@PAA@NHS/*A. succinogenes* group relative to the pristine *A. succinogenes*, whereas it exhibited a 78% decrease in the NiO@PAA@NHS/Au@*A. succinogenes* group, as shown in Fig. 4d. This observed change is largely due to the conversion of NADH to NAD^+ during

the metabolic pathways leading to succinic acid production. Key enzymes in these pathways, including malate dehydrogenase (MDH), fumarase (FUM), and fumarate reductase (FRD), are involved in the oxidation of NADH to NAD^+. Therefore, to direct the bacterial metabolism towards the C_4 pathway for succinic acid synthesis, an increased production of NAD^+ is necessary, which is facilitated by the PEC process.

To further unravel the mechanisms underlying succinic acid production in different systems, we analyzed the expression levels of key genes associated with mixed-acid synthesis using real-time quantitative reverse transcription polymerase chain reaction (RT-PCR) (Fig. 4e). Overall, upon attachment to the electrode, the expression of all genes in *A. succinogenes* was upregulated, indicating that efficient electron supply at the electrode modulates an increase in various metabolic gene products. This upregulation was observed in both the NiO@PAA@NHS/A. succinogenes and NiO@PAA@NHS/Au@*A. succinogenes* systems. PEPCK and PK are determinants of the C4 and C3 pathways, respectively, while FRD, PflB, and ACK correspond to the production of succinic acid, formic acid, and acetic acid, respectively. Despite the significant upregulation of PK, which is associated with pyruvate kinase, the concentration of pyruvate remained low (Supplementary Fig. 27a). Meanwhile, the product distribution analysis revealed a notable shift in metabolic selectivity upon system modification. For *A. succinogenes*, succinic acid accounted for merely 44% of total products, while integration of the electrode assembly elevated this proportion to 52% (Supplementary Fig. 27b). These findings indicate that the Au NPs coupled with the photoelectrode not only

enhanced the succinic acid production kinetics but also improved its metabolic selectivity. Although the concentrations of acetic and formic acids increased, succinic acid remained the predominant product. This suggests that pyruvate in the system is primarily converted into oxaloacetate and then funneled through the C_4 pathway to produce succinic acid.

Discussion

In summary, the *A. succinogenes* after Au NPs-ALE with a NiO@PAA@NHS photoelectrode has resulted in the successful construction of a photoelectrocatalytic-microbial biohybrid system, NiO@PAA@NHS/Au@*A. succinogenes*. Notably, while the PAA@NHS hydrogel enables robust bacterial adhesion, conclusive evidence for covalent bonding remains elusive and merits further investigation. This system capitalizes on the synergistic interaction between the conductive properties of Au NPs and the metabolic capabilities of *A. succinogenes* to enhance charge transfer and drive the conversion of CO_2 into succinic acid under solar illumination. The Au-ALE process of *A. succinogenes* facilitated the internalization of Au NPs, which served as an efficient intracellular charge transfer pathway, thereby improving the bacteria's ability to utilize photogenerated electrons from the NiO@PAA@NHS photoelectrode. This innovative approach has led to a marked increase in succinic acid production rates, achieving a yield of 1.41 ± 0.04 g L^{-1} h^{-1} cm^{-2} (0.012 ± 0.0003 mol mol L^{-1} h^{-1} cm^{-2}), which is significantly higher than conventional fermentation methods. The biohybrid system demonstrated excellent long-term stability and biocompatibility, maintaining

consistent succinic acid production over extended periods, and simulating natural light-dark cycles. These attributes, combined with the system's high yield rates and contributions to carbon neutrality, position the NiO@PAA@NHS/Au@*A. succinogenes* biohybrid as a leading candidate for sustainable and efficient large-scale succinic acid production. This study presents a groundbreaking approach that merges nanotechnology with microbial biology to create a sustainable platform for chemical synthesis. The NiO@PAA@NHS/Au@A. succinogenes biohybrid system exemplifies the potential of leveraging renewable energy to drive bioprocesses, offering a promising avenue for the development of eco-friendly production methods in the chemical industry. Recent technological advances in reactor design, light management, and process optimization provide a promising pathway for the industrialization of photo-biohybrid systems [54-57], although challenges such as ensuring uniform illumination, efficient mixing, and stable long-term operation must still be addressed to achieve scalable and sustainable production.

Methods

Strains and Media. *Actinobacillus succinogenes* 130Z (ATCC 55618) was obtained from Professor Wenming Zhang (Nanjing Tech University). The culture medium contained: 5 g/L yeast extract, 9.6 g/L $NaH_2PO_4 \cdot 2H_2O$, 15.5 g/L $K_2HPO_4 \cdot 3H_2O$, 10 g/L $NaHCO_3$, 30 g/L glucose, 1 g/L NaCl, and 2.5 g/L corn steep liquor at 37°C and 170 rpm. The fermentation medium consisted of 10 g/L yeast extract, 1.36 g/L NaAc, 0.3 g/L $Na_2HPO_4 \cdot 12H_2O$, 1.6 g/L $Na_2HPO_4 \cdot 2H_2O$, 3 g/L K_2HPO_4, 1 g/L NaCl, 0.2 g/L $MgCl_2 \cdot 6H_2O$, 7.5 g/L corn steep liquor, 0.2 g/L $CaCl_2$ and 15 g/L $Mg_2(OH)_2CO_3$ for PH neutralizer. Glucose was added after sterilization at a concentration of 30g/L

for fermentation.

Preparation of NiO photocathode. NiO photocathodes were synthesized using a hydrothermal method. Firstly, nickel foam (Ni Foam) was cut into electrode sheets of 1 × 5 cm size, and sequentially cleaned with acetone, alcohol, and distilled water by ultrasonic cleaning for 15 min. the whole NF was directly immersed into a 3 M HCl aqueous solution at 90 °C for 20 min in a static immersion to remove surface oxides. The NF was washed with distilled water and the washed NF was dried under nitrogen. Next, $Ni(NO_3)_2 \cdot 6H_2O$ (1 mmol) and urea (2 mmol) were dissolved in distilled water (15 mL) and stirred to form a green transparent solution. The pretreated NF (1 cm × 5 cm) was immersed in the solution in a Teflon reactor (25 mL) and kept at 100 °C for 12 h. The electrodes were then removed and the electrodes were placed in a water bath. After removing the electrodes, they were ultrasonically cleaned in ethanol and distilled water. Finally, the electrodes were calcined in a muffle furnace under air atmosphere at 250 °C for 3 h.

Preparation of NiO@PAA@NHS photocathode. First, the NiO NSs electrodes were immersed in an aqueous acrylic acid solution (30% w/w acrylic acid, 0.03% w/w N,N'-bis(acryloyloxy)cysteamine and 0.15 % w/w 2,2'-azobis(2-methylpropionamidine) dihydrochloride) for 2 h. Then, the immersed hydrogel was sealed and heated at 70 °C for 30 min to form the PAA network, and finally dried under nitrogen flow. Subsequently, the prepared NiO@PAA NSs electrode was placed in a mixture of 1-ethyl-3-(-3-dimethylaminopropyl) carbodiimide (0.5% w/w) and N-hydroxylthiosuccinimide (0.25% w/w) aqueous solution and soaked for 5 min at room temperature, and then the hydrogel was further dried to obtain the NiO@PAA@NHS NSs photocathode.

Au-ALE of *Actinobacillus succinogenes.* $HAuCl_4$ solution was first added to 20 mL of culture solution to reach a concentration of 0.5 μM. After 12 h of incubation, the bacteria were inoculated into a new 20 mL culture solution, and $HAuCl_4$ solution was added to make the concentration of $HAuCl_4$ of 1.0 μM, 1.5 μM, and 2.0 μM to complete the ALE process. Bacterial cultivation was conducted for 12 hours under each $HClO_4$ concentration.

Construction of NiO@PAA@NHS/Au@*A. succinogenes* biohybrid. Different Au-ALE concentrations of *Au@A.succinogenes* were inoculated in 20 mL of culture broth, and $HAuCl_4$ solution was added to make the concentrations 1 μM, 2 μM, 3 μM, and 4 μM, respectively. The bacteria were incubated anaerobically in a shaker at 37 °C for 12 h. Subsequently, 10,000 g centrifugation was performed to collect the *Au@A.succinogenes*, and the culture broth was washed with 0.1 M phosphate buffered saline (PBS) washed three times to remove the medium, which was dispersed again in the fermentation broth, and the prepared NiO@PAA@NHS photocathode was placed in solution and incubated for 2 h to construct the NiO@PAA@NHS/*Au@A. succinogenes* hybrid photoelectrode.

Bacteria density on photoelectrode. High-resolution SEM images were acquired from five randomly selected fields of view on each electrode surface. The images were analyzed using ImageJ software, where bacterial cells were identified through threshold segmentation, followed by manual correction to ensure accuracy. The actual surface area of each field was calculated based on the scale bar, and bacterial counts were normalized accordingly to yield cells per mm^2. The reported data represent the mean ± standard deviation of five independent regions.

Photoelectrochemical measurements. The photocatalytic test was completed with a three-electrode system, the reference electrode (RE) was Ag/AgCl, the counter electrode (CE) was a platinum electrode, the working electrode (WE) was a biohybrid photoelectrode prepared as described in **Construction of NiO@PAA@NHS/Au@*A. succinogenes* biohybrid**, and the electrolyte was a bacterial fermentation broth. The reaction was carried out in a 100 mL reactor with a 50 mL working volume. The potential of the saturated Ag/AgCl was converted to that of the reversible hydrogen electrode (RHE) as follows in all the experiments:

$$E_{RHE}\ (V) = E_{Ag/AgCl} + 0.059 \times pH + 0.1976 \qquad (1)$$

CO_2 was passed 30 min before the start of the reaction to remove dissolved oxygen. LSV and I-t curve are performed on an Autolab PGATAT302N (Metrohm, Switzerland) electrochemical workstation. For H_2 supplementation controls, H_2 gas was continuously supplied at 400 mL h^{-1}

during operation. The PEC-biohybrid experiments were performed at an applied potential of −0.3 V versus RHE under illumination, whereas the biohybrid controls were operated in the dark under open-circuit conditions. All other experimental conditions were kept identical to those without external H_2. Succinic acid production was quantified by HPLC.

Preparation of the thin-sectioned samples of the hybrid system. The cultured samples were harvested by centrifugation at 10000 rpm for 10 min and washed three times with 0.1 M phosphate-buffered saline (PBS) to remove culture solution before further characterization. For sample preparation, the hybrid system was dissolved in 1 mL of PBS solution and then fixed using 4% glutaraldehyde at 4 °C. After 2 h of fixation, the sample was washed twice with PBS solution at room temperature, then stained with fresh 1% OsO_4 in PBS for 1 h. After washing two times with PBS, the sample was sequentially dehydrated in 50%, 70%, 85%, 95% (two times), and 100% (three times) acetone, each time lasting for 10-15 min. Part of the dehydrated sample was embedded and sequentially infiltrated with 1:2, 1:1, and 3:1 resin:acetone, followed by pure resin for three times. The sample was further baked at 70 °C for 12 h for complete curing and cut into 70 nm thin sections with a diamond knife. Finally, the sample was deposited onto a Formvar coated copper grid and microscope slide for transmission electron microscopy and confocal fluorescent observation, respectively.

Biohybrid photoelectrode characterizations. Scanning electron microscopy (SEM) images were viewed with a Hitachi-S4800 scanning electron microscope. Transmission electron Microscope (TEM) images were viewed with a JEOL JEM-2100 scanning electron microscope. UV–vis absorption spectrum was recorded on an evolution 789S spectrophotometer (Shanghai light Technology Company). Confocal laser scanning microscopy (CLSM) images were obtained by a confocal laser scanning microscope (TCS SP8 MP SMD, LEICA, German). The light source was derived from a Xenon lamp (PLS-SXE300, Perfect Light, Beijing) with a filter (AM 1.5G, Perfect Light, Beijing).

Analytical methods. The concentrations of organic acids were determined using Shimadzu high-

performance liquid chromatography (Japan). Separation of the samples was achieved using an Ion exclusion chromatography column (Shim-pack SCR-101H) under the following conditions: a column temperature of 55 °C, a mobile phase of 100% 0.25 g/L H_2SO_4, and a flow rate of 0.5 mL/min. Succinic acid, pyruvic acid, formic acid, and acetic acid were detected were detected at 214 nm using an SPD-20A detector. An automatic sampler was used to inject 20 μL of the samples into the chromatograph.

Determination of CO_2 conversion efficiency. CO_2 flow rate was monitored continuously with a calibrated mass-flow meter and fixed at 7 mL min^{-1} (at 298 K and 1 atm). The molar CO_2 feed rate was therefore:

$$\dot{n}_{(CO_2,\ input)} = 7\ mL\ min^{-1} \div 24450\ mL\ mol^{-1} \times t(min) = 2.86 \times 10^{-4}\ t\ mol \quad (2)$$

Succinic acid was detected by HPLC; its molar yield was quantified at different reaction durations. The CO_2 conversion efficiency was then calculated as:

$$CO_2\ \text{Conversion Rate}\ (\%) = \left(\frac{\text{Succinic Acid Yield(mol)}}{CO_2\ \text{Input (mol)}}\right) \times 100\% \quad (3)$$

Glucose concentration analysis. The glucose level was measured using the Beyotime Glucose Assay Kit with O-toluidine, which is based on the chromogenic reaction between glucose and o-toluidine, with quantification performed by colorimetric analysis.

Faradaic efficiency calculation. The Faradaic efficiencies (FEs) for gaseous products were calculated based on the total charge passed during PEC and the quantified number of products formed. The total charge Q (C) was obtained by integrating the photocurrent over the reaction time, and the molar amount of each product n (mol) was determined from gas chromatography (GC) or high-performance liquid chromatography (HPLC) analysis. The FE for each product was calculated using the following equation:

$$FE = n \times z \times F \div Q \times 100\% \quad (4)$$

Where n is the number of moles of the detected product, z is the number of electrons transferred per molecule (2 for both H_2 and CO), and F is the Faraday constant (96485 C mol^{-1}).

Cyclic voltammetry measurements. Cyclic voltammetry (CV) was performed in a three-

electrode configuration using carbon paper (1 × 1 cm^2) as the working electrode, a Pt foil/wire as the counter electrode, and a saturated Ag/AgCl electrode as the reference electrode. The electrolyte was 10 mM phosphate-buffered saline (PBS, pH 7), deaerated with CO_2 for 30 min prior to measurements and maintained under a continuous CO_2 atmosphere. All measurements were conducted at 37 °C. Wild-type and Au@A. succinogenes cells were harvested by centrifugation, washed three times with PBS, and resuspended to $OD_{600} \approx 2.0$. The carbon paper was immersed in the bacterial suspension and incubated anaerobically at 37 °C for 4 h to allow cell attachment, then gently rinsed with PBS and used immediately. CV was recorded in the potential range of -0.4 V to 1.4 V (vs RHE) at scan rates of 5–50 mV s^{-1}. Each voltammogram represents a stable response after 3 consecutive scans. Measurements were repeated with independently prepared bacterial suspensions (n = 3). Cell-free supernatants were tested under identical conditions as controls.

NAD^+/NADH assay kit measurements. NAD^+ /NADH assay kit (Beyotime Biotechnology) with WST-8 was used to determine the concentration of NADH and NAD^+ in *A. succinogenes* following the standard manual of the assay kit. All experiments were conducted in the same fermentation broth under identical anaerobic conditions; control and biohybrid samples were cultured for the same duration, with the latter operated under light illumination and applied potential.

Measurement of ATP content. First, 200 μL lysate was gently added to promote cell lysis, and centrifuged at 12000 g for 5 min to obtain supernatant solution. Then, 100 μL ATP detection solution was added to the 96-well plate in advance to consume background ATP, and placed at room temperature for 3 minutes. After adding 100 μL sample, and the RLU value was determined by luminometer.

***A. succinogenes* viability.** During the long-term test, the viability of *A.succinogenes* has been determined by colony-forming units (CFU) assays. At fixed time intervals, aliquots of 500 μL reaction solution was collected by a sealing syringe. 100 μL of the collected sample was serially diluted with saline. 100 μL of the original and diluted sample were spread on sterilized nutrient

agar plates, then incubated at 37 °C for 12 h. Finally, the survival number of cells (in CFU) was quantified by counting the visible colonies and the survival rate was calculated.

Staining Analysis of Bacteria. The bacteria before and after reactions were resuspended in 100 μL BBcellProbe N01 Dye solution A and PI Dye solution B. After incubating at room temperature for 15 min, the bacteria were washed with 0.85% NaCl solution once and then suspended again. Finally, add 20 μL bacterial to the confocal surface dish and the samples were imaged with CLSM under the excited laser of 488 nm, the emission wavelength of 525 and 620 nm respectively.

Flow Cytometry Analysis. *A. succinogenes* cells were harvested, washed, and resuspended in phosphate-buffered saline (PBS, pH 7.4) prior to measurement. All samples were analyzed using a CytoFLEX flow cytometer (Beckman Coulter, Inc., Brea, CA, USA) equipped with 488 nm and 638 nm lasers. Forward scatter (FSC) and side scatter (SSC) were used to gate bacterial populations based on size and granularity, and a threshold was set on SSC to exclude debris and electronic noise. A minimum of 50,000 events per sample were recorded within the bacterial gate. Data acquisition was performed using CytExpert software (version 2.4, Beckman Coulter), and all collected flow cytometry standard (FCS) files were subsequently analyzed with FlowJo software (version 10.8, BD Biosciences, San Jose, CA, USA). The analysis included gating on singlets, exclusion of outliers, and quantification of fluorescence-positive subpopulations based on unstained and single-stained controls. All experiments were performed in at least three independent biological replicates, and representative histograms or dot plots are shown.

Quantitative RT-PCR. Total RNA Extractor（Trizol）was used to extract total RNA. Real-time quantitative PCR technology refers to the experimental method of quantitative analysis of the starting template by adding a fluorescent group (SYBR green I) to the PCR reaction system, and using the accumulation of fluorescent signals to monitor the PCR process in real time. The 16S rRNA gene was used to standardize the mRNA levels. Primer sequences for qRT-PCR are indicated in Supplementary Table 3. The mRNA level of the target genes was calculated via the $2^{-\Delta\Delta CT}$ method.

Statistics. Statistical analysis was performed using GraphPad Prism 8.0.2 software using a two-tailed t test analysis of variance hypothesis. Significant differences are marked as *P < 0.05, **P < 0.01, and ***P < 0.001. All data are presented as mean ± SD. The number of biologically independent samples for each panel was three unless otherwise stated in the figure legends.

Data availability

Data supporting the findings of this work are available within the paper and its Supplementary Information files. Source data are provided with this paper.

References

1. Kim, J. Y., Lee, J. A., Ahn, J. H. & Lee, S. Y. High-level succinic acid production by overexpressing a magnesium transporter in *Mannheimia succiniciproducens*. *Proc. Natl. Acad. Sci*. **121**, e2407455121 (2024).
2. Cui, Z. et al. Reconfiguration of the reductive TCA cycle enables high-level succinic acid production by *Yarrowia lipolytica*. *Nat. Commun*. **14**, 8480 (2023).
3. Kaur, R. & Chauhan, I. Biodegradable plastics: mechanisms of degradation and generated bio microplastic impact on soil health. *Biodegradation* **35**, 863-892 (2024).
4. Kumar, V. et al. Recent advances in bio-based production of top platform chemical, succinic acid: an alternative to conventional chemistry. *Biotechnol. Biofuels Bioprod.* **17**, 72 (2024).
5. Tran, V. G. An end-to-end pipeline for succinic acid production at an industrially relevant scale using *Issatchenkia orientalis*. *Nat. Commun*. **14**, 6152 (2023).
6. Narisetty, V. et al. Technological advancements in valorization of second generation (2G) feedstocks for bio-based succinic acid production. *Bioresour. Technol.* **360**, 127513 (2022).
7. Dickson, R. et al. Sustainable bio-succinic acid production: superstructure optimization, techno-economic, and lifecycle assessment. *Energy Environ. Sci*. **14**, 3542–3558 (2021).
8. Guan, X., Yu, Y. & Zhang, M. Theoretical Insights into the Reaction Mechanism of Direct Hydrogenation of Maleic Anhydride to Produce 1,4-Butanediol on the Cu–ZnO Surface. *ACS Catal* **14**, 6488–6502 (2024).
9. Lin, F. et al. Advances in succinic acid production: the enhancement of CO_2 fixation for the carbon sequestration benefits. *Front. Bioeng. Biotechnol*. **12**, 1392414 (2024).
10. Bello, S. et al. Renewable carbon opportunities in the production of succinic acid applying attributional and consequential modelling. *Chem. Eng. J*. **428**, 132011 (2022).
11. Yang, Y. et al. Progress on production of succinic acid by *Actinobacillus succinogenes*-new opportunities for cheap biomass and waste gas utilization. *J. Clean. Prod.* **434**, 140005 (2024).
12. Pinazo, J. M., Domine, M. E., Parvulescu, V. & Petru, F. Sustainability metrics for succinic acid production: A comparison between biomass-based and petrochemical routes. *Catal.*

Today **239**, 17–24 (2015).
13. Liang, G. et al. Designing a periplasmic photosynthetic biohybrid system for succinate and electric energy production. *Chem. Eng. J*. **477**, 147152 (2023).
14. Ahn, J. H. et al. Enhanced succinic acid production by *Mannheimia* employing optimal malate dehydrogenase. *Nat. Commun*. **11**, 1970 (2020).
15. Dessie, W. et al. Opportunities, challenges, and future perspectives of succinic acid production by *Actinobacillus succinogenes*. *Appl. Microbiol. Biotechnol.* **102**, 9893–9910 (2018).
16. Pateraki, C. et al. *Actinobacillus succinogenes*: Advances on succinic acid production and prospects for development of integrated biorefineries. *Biochem. Eng. J.* **112**, 285–303 (2016).
17. Mokwatlo, S. C., Nicol, W. & Brink, H. G. Internal mass transfer considerations in biofilms of succinic acid producing *Actinobacillus succinogenes*. *Chem. Eng. J.* **407**, 127220 (2021).
18. Chen, C., Zheng, P. New Insights into the Biosynthesis of Succinic Acid by Actinobacillus succinogenes with the Help of Its Engineered Strains. *Fermentation*, **9**, 1026 (2023).
19. Bradfield, M. F. A., Nicol, W. The pentose phosphate pathway leads to enhanced succinic acid flux in biofilms of wild-type *Actinobacillus succinogenes*. *Appl. Microbio. Biotechnol.* **100**, 9641-9652 (2016).
20. McKinlay, J. B., Shachar-Hill, Y., Zeikusa, J. G., Vieille, C. Determining Actinobacillus succinogenes metabolic pathways and fluxes by NMR and GC-MS analyses of ^{13}C-labeled metabolic product isotopomers. *Metab. Eng*. **9**, 177-192 (2007).
21. McKinlay, J. B., Vieille, C. ^{13}C-metabolic flux analysis of Actinobacillus succinogenes fermentative metabolism at different $NaHCO_3$ and H_2 concentrations. *Metab. Eng*. **10**, 55-68 (2008).
22. McKinlay, J. B. et al. A genomic perspective on the potential of Actinobacillus succinogenes for industrial succinate production. *BMC Genomics* **11**, 680 (2010).
23. Gong, F., Li, Y. Fixing carbon, unnaturally. *Science* **354**, 830-831 (2016).
24. Steffens, L. et al. High CO_2 levels drive the TCA cycle backwards towards autotrophy. *Nature* **592**, 784–788 (2021).
25. Hu, G. et al. Light-driven CO_2 sequestration in *Escherichia coli* to achieve theoretical yield of chemicals. *Nat. Catal*. **4**, 395–406 (2021).
26. Guo, M. et al. Abiotic-biotic interfaces and electron transfer pathways in nanomaterial-microorganism biohybrids for efficient CO_2 conversion. *J. Environ. Chem. Eng*. **12**, 112794 (2024).
27. Zhan, C. et al. Reprogramming methanol utilization pathways to convert Saccharomyces cerevisiae to a synthetic methylotroph. *Nat. Catal.* **6**, 435–450 (2023).
28. Mitchell, J. H., Freedman, A. H., Delaney, J. A. & Girguis, P. R. Co-expression analysis reveals distinct alliances around two carbon fixation pathways in hydrothermal vent symbionts. *Nat. Microbiol*. **9**, 1526–1539 (2024).
29. Chen, H., Dong, F. & Minteer, S. D. The progress and outlook of bioelectrocatalysis for the production of chemicals, fuels and materials. *Nat. Catal.* **3**, 225–244 (2020).

30. Wang, R. et al. Nanomaterials Facilitating Microbial Extracellular Electron Transfer at Interfaces. *Adv. Mater.* **33**, 2004051 (2021).
31. Cestellos-Blanco, S., Zhang, H., Kim, J. M., Shen, Y. X., Yang, P. Photosynthetic semiconductor biohybrids for solar-driven biocatalysis. *Nat. Catal.* **3**, 245-255 (2020).
32. Han, H. X. et al. Reversing Electron Transfer Chain for Light-Driven Hydrogen Production in Biotic–Abiotic Hybrid Systems. *J. Am. Chem. Soc*. **144**, 6434–6441 (2022).
33. Yu, Y. Y. et al. Single cell electron collectors for highly efficient wiring-up electronic abiotic/biotic interfaces. *Nat. Commun*. **11**, 4087 (2020).
34. Chen, X. et al. 3D-printed hierarchical pillar array electrodes for high-performance semi-artificial photosynthesis. *Nat. Mater.* **21**, 811–818 (2022).
35. Fang, X., Kalathil, S., Divitini, G., Wang, Q. & Reisner, E. A three-dimensional hybrid electrode with electroactive microbes for efficient electrogenesis and chemical synthesis. *Proc. Natl. Acad. Sci. U. S. A.* **117**, 5074–5080 (2020).
36. Luo, H. et al. Chemical reaction-mediated covalent localization of bacteria. *Nat. Commun*. **13**, 7808 (2022).
37. Ming, Z. et al. Living Bacterial Hydrogels for Accelerated Infected Wound Healing. *Adv. Sci*. **8**, 2102545 (2021).
38. Tang, T. C. et al. Hydrogel-based biocontainment of bacteria for continuous sensing and computation. *Nat. Chem. Biol.* **17**, 724–731 (2021).
39. Kim, J., Cestellos-Blanco, S., Shen, Y., Cai, R. & Yang, P. Enhancing Biohybrid CO_2 to Multicarbon Reduction via Adapted Whole-Cell Catalysts. *Nano Lett*. **22**, 5503–5509 (2022).
40. Zhang, H. et al. Bacteria photosensitized by intracellular gold nanoclusters for solar fuel production. *Nat. Nanotechnol*. **13**, 900–905 (2018).
41. Chen, Z. & Rozhkova, E. A. Intracellular gold nanoclusters boost energy conversion. *Nat. Nanotechnol*. **13**, 880–881 (2018).
42. Hu, Q. et al. Ultrafast Electron Transfer in Au–Cyanobacteria Hybrid for Solar to Chemical Production. *ACS Energy Lett*. **8**, 677–684 (2023).
43. Correa-Llantén, D. N., Muñoz-Ibacache, S. A., Castro, M. E., Muñoz, P. A., Blamey, J. M. Gold nanoparticles synthesized by Geobacillus sp. strain ID17 a thermophilic bacterium isolated from Deception Island, Antarctica. Microb. Cell. Fact. **12**, 75 (2013).
44. Dhanasekar, N. N., Shirke, A., Sakthivel, N. Bioreduction of Gold Ions from Anisotropic to Isotropic Nanostructures by NADPH-Dependent Reductase from *Bipolaris oryzae*. *ChemistrySelect* **5**, 11522-11529 (2020).
45. Chen, X., Yuk, H., Wu, J., Nabzdyk, C. S. & Zhao, X. Instant tough bioadhesive with triggerable benign detachment. *Proc. Natl. Acad. Sci. U. S. A.* **117**, 15497–15503 (2020).
46. Alberts, E. M. et al. Toward bioinspired polymer adhesives: activation assisted via HOBt for grafting of dopamine onto poly(acrylic acid). *R. Soc. Open Sci* **9**, 211637 (2022).
47. Faghihzadeh, F., Anaya, N. M., Schifman, L. A., Oyanedel-Craver, V. Fourier transform infrared spectroscopy to assess molecular-level changes in microorganisms exposed to

nanoparticles. *Nanotechnol. Environ. Eng*. **1**, 1 (2016).
48. Yang, J. et al. Novel Modification of Collagen: Realizing Desired Water Solubility and Thermostability in a Conflict-Free Way. *ACS Omega* **5**, 5772–5780 (2020).
49. Khalil, M. et al. Suppressing the competing hydrogen evolution reaction in CO_2 electroreduction: A review. Renew. Sustain. Energy Rev. 206, 114869 (2024).
50. Ren, L. et al. Construction of high selectivity and antifouling nanofiltration membrane via incorporating macrocyclic molecules into active layer. *J. Membr. Sci.* **597**, 117641 (2020).
51. Pateraki, C. et al. Transcriptional regulation in key metabolic pathways of *Actinobacillus succinogenes* in the presence of electricity. *Bioelectrochemistry* **151**, 108376 (2023).
52. Safarian, S. et al. Structure of a bd oxidase indicates similar mechanisms for membrane-integrated oxygen reductases. *Science* **352**, 583–586 (2016).
53. Zhang, Y., Feng, T., Zhou, X., Zhang, Z. Photoelectrocatalytic-Microbial Biohybrid for Nitrogen Reduction. *Adv. Mater.* **36**, 2407239 (2024).
54. Huang, Q., Jiang, F., Wang, L. & Yang, C. Design of Photobioreactors for Mass Cultivation of Photosynthetic Organisms. *Engineering* **3**, 318–329 (2017).
55. Peter, A. P. et al. Continuous cultivation of microalgae in photobioreactors as a source of renewable energy: Current status and future challenges. *Renew. Sustain. Energy Rev*. **154**, 111852 (2022).
56. Wang, Y., Tahir, N., Cao, W., Zhang, Q. & Lee, D. J. Grid columnar flat panel photobioreactor with immobilized photosynthetic bacteria for continuous photofermentative hydrogen production. *Bioresour. Technol*. **291**, 121806 (2019).
57. Palamae, S. et al. Production of renewable biohydrogen by Rhodobacter sphaeroides S10: A comparison of photobioreactors. *J. Clean. Prod*. **181**, 318–328 (2018).

Acknowledgments

This research was supported by National Natural Science Foundation of China (No. 2274041, Z. Z.).

Author contributions

T. F., X. Z. and Z. Z. designed the experiments. T. F., Y. Z. and X. Z. carried out the experiments. X. Z. conducted the characterizations. All authors wrote the manuscript.

Competing interests

The authors declare no competing interests.

Figure legends

Fig. 1 | PEC-bacterial biohybrid system. (a) Schematics of the PEC-bacterial reactor for succinic acid generation; (b) schematics of interfacial connections in NiO@PAA@NHS/Au@*A. succinogenes* biohybrid. The diagrams were created using Adobe Illustrator.

Fig. 2 | Visual representation of bacterial adhesion and Au NPs integration. (a) Schematic illustration of Au-ALE of *A. succinogenes*; (b) TEM image of thin-sectioned wild type *A. succinogenes*, the scale bar is 200 nm; (c) TEM image of thin-sectioned *A. succinogenes* after Au-ALE (Au@*A. succinogenes*), the scale bar is 200 nm; (d) HAADF-STEM image of thin-sectioned Au@*A. succinogenes*, the scale bar is 200 nm; (e) EDS mapping image of Au in Au@*A. succinogenes*, the scale bar is 200 nm; the TEM images are representative of results obtained from at least three independent experiments with similar outcomes; (f) fluorescence intensity in flow cytometry with gated events of *A. succinogenes* culturing in high concentration of Au ion (2 μM) and culturing in gradient ALE process (0.5 μM, 1 μM, 1.5 μM, and 2 μM); (g) schematic illustration of the interaction between NiO@PAA@NHS and Au@*A. succinogenes* bacteria; (h) SEM image of NiO/Au@*A. succinogenes*, the scale bar is 1 μm; (i) SEM image of NiO@PAA@NHS/Au@*A. succinogenes*, the scale bar is 1 μm; (j) cellular density measurements of Au@*A. succinogenes* on bare NiO and on NiO@PAA@NHS, expressed as cell counts per square millimeter (10^6/mm^2), data are represented as mean ± SD (n=3) and statistical analysis is performed using a two-tailed Student's t-test, ***P < 0.001. The diagrams in panels a and g were created using Adobe Illustrator. Source data for this figure is available in the Source Data file

Fig. 3 | Performance of PEC-bacterial biohybrids. (a) LSV curves of NiO@PAA@NHS/Au@*A. succinogenes* hybrid in dark or under illumination in Ar or CO_2 saturated electrolytes; (b) succinic acid yield rate with different reaction models of PEC-biohybrid (-0.3 V vs RHE), EC-biohybrid (-0.3 V vs RHE in dark), PC-biohybrid, and pristine biohybrid in dark under open circuit condition, the operation duration was 24 h; (c) succinic acid yield rate in PEC model on NiO, NiO@PAA@NH, NiO@PAA@NHS/*A. succinogenes*, and NiO@PAA@NHS/Au@*A. succinogenes* under illumination of solar light, the operation duration was 24 h; (d) time-dependent current densities of biohybrid system at various applied potentials; (e) succinic acid yield rate on NiO@PAA@NHS/Au@*A. succinogenes* photoelectrode at different applied potentials, the operation duration was 24 h; (f) yields of succinic acid and by-products of acetic acid, formic acid, and pyruvic acid after PEC-bacterial reaction; (g) long-term succinic acid generation on NiO@PAA@NHS/Au@*A. succinogenes* biohybrid in alternating PEC and EC models at -0.3 V vs RHE; (h) comparison of succinic acid yield rates of different bacteria and reaction models,

including the Microbial Fermentation (MF) reactor system. Data are represented as means ± SD (n=3). Source data for this figure is available in the Source Data file.

Fig. 4 | Mechanism of succinic acid generation in biohybrid. (a) Schematic illustration of the extracellular-intracellular electron uptake and succinic acid production mechanism of NiO@PAA@NHS/Au@*A. succinogenes* biohybrid; (b) fluorescence lifetime spectra in *A. succinogenes* and Au@*A. succinogenes*; (c) relative ATP level of after and before reaction in *A. succinogenes,* NiO@PAA@NHS/*A. succinogenes,* and NiO@PAA@NHS/Au@*A. succinogenes*; (d) NADH/NAD^+ ratios in *A. succinogenes,* NiO@PAA@NHS/*A. succinogenes,* and NiO@PAA@NHS/Au@*A. succinogenes*; (e) relative mRNA expression level of PK, PEPCK, FRD, PflB, and ACK in *A. succinogenes,* NiO@PAA@NHS/*A. succinogenes,* and NiO@PAA@NHS/Au@*A. succinogenes*. Data are represented as mean ± SD (n=3) and statistical analysis is performed using a two-tailed Student's t-test, *$P < 0.05$, **$P < 0.01$, and ***$P < 0.001$), ns, not significant. Source data for this figure is available in the Source Data file.

Editorial Summary

Succinic acid is platform chemical produced by energy-intensive and environmentally unfriendly means. To unlock a biological route, the authors alleviate the limited intracellular electron transfer in A. succinogenes via a photoelectrocatalytic biohybrid, achieving a production rate of 1.41 g L-1 h-1 cm-2.

Peer review information: *Nature Communications* thanks Santiago Rodriguez Jimenez, and the other, anonymous, reviewer(s) for their contribution to the peer review of this work. A peer review file is available.

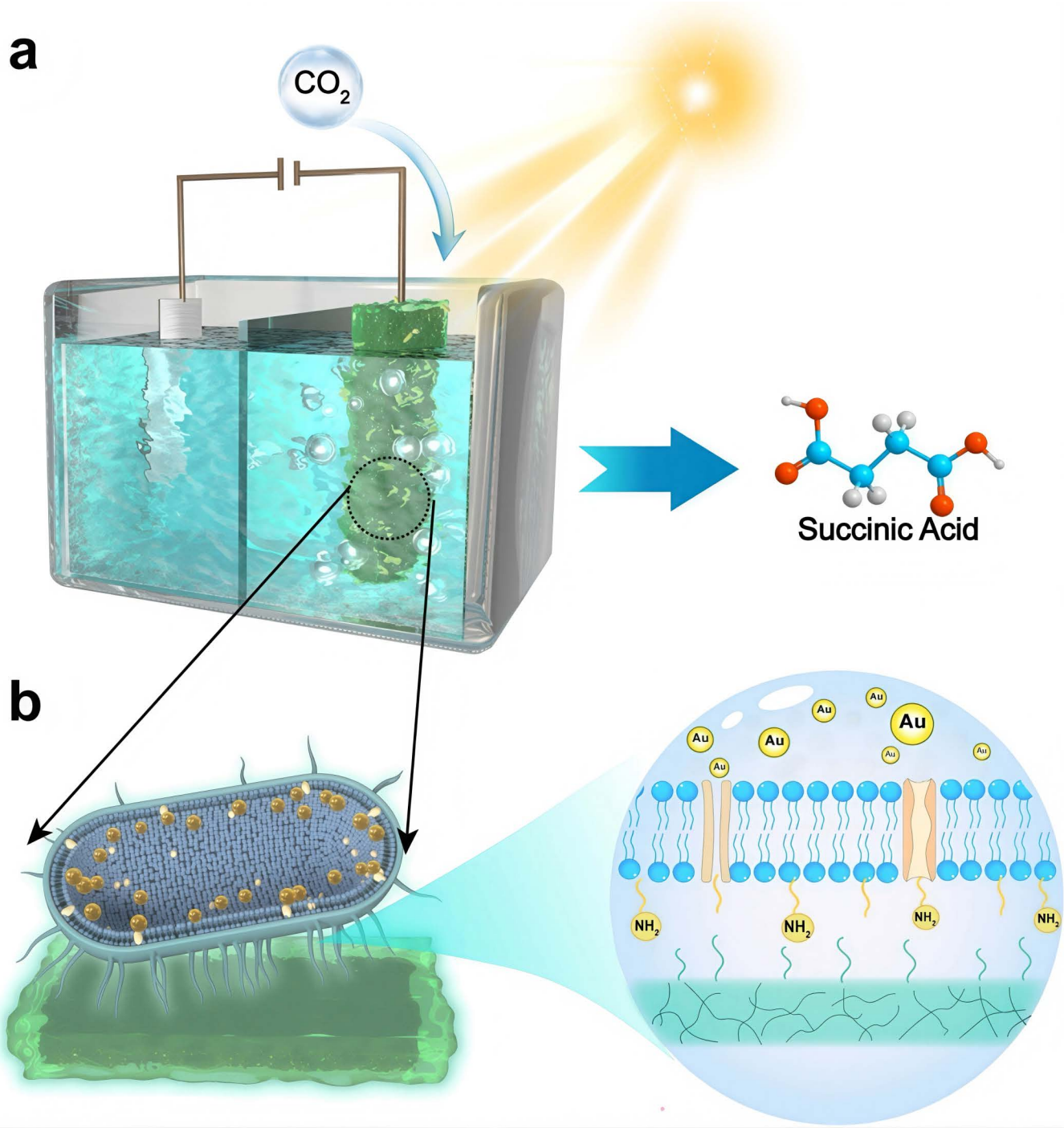
a
CO_2
Succinic Acid
b
Au
NH_2

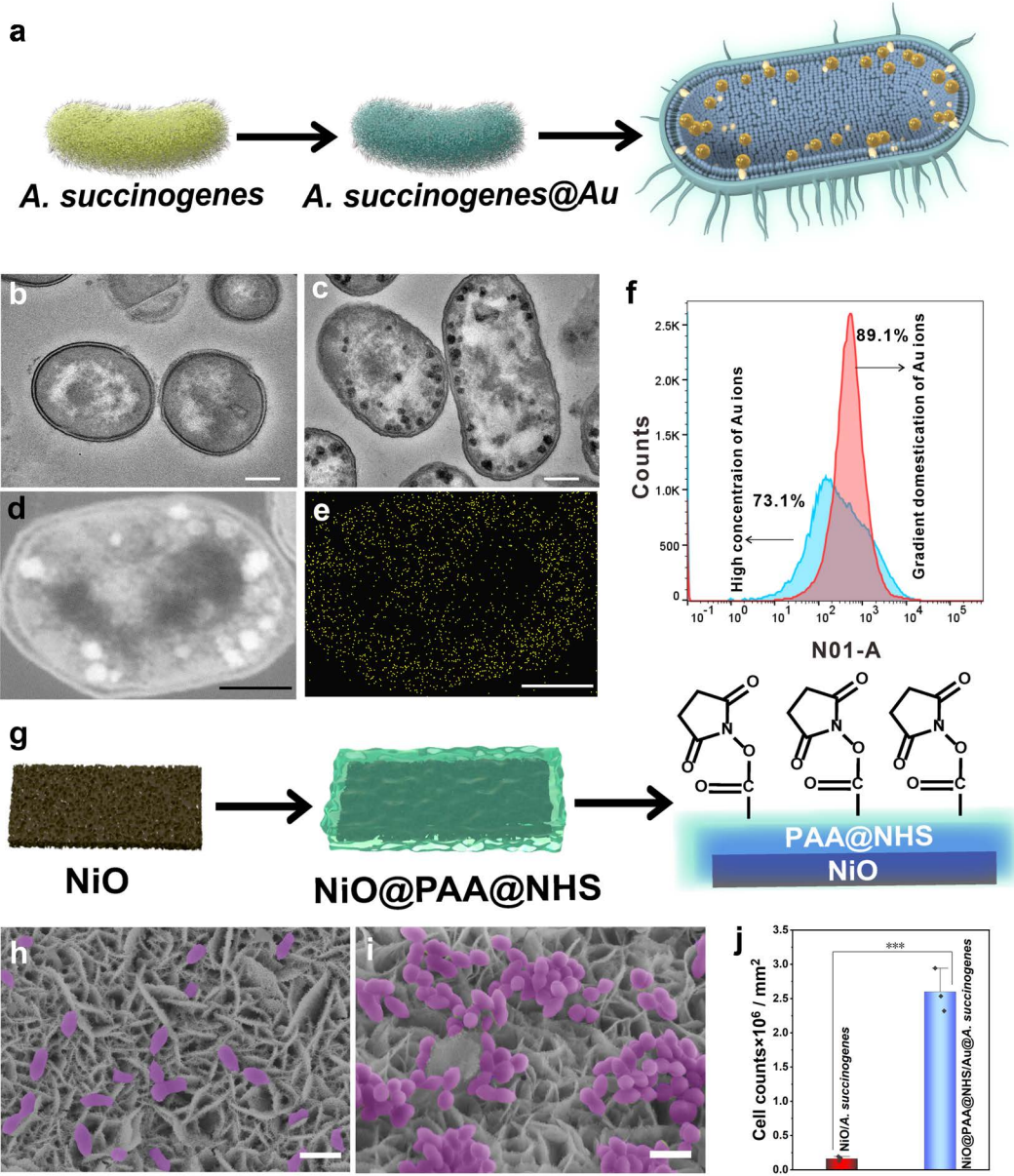
a
A. succinogenes
A. succinogenes@Au
b
c
d
e
f
89.1%
73.1%
High concentraion of Au ions
Gradient domestication of Au ions
Counts
N01-A
g
NiO
NiO@PAA@NHS
PAA@NHS
NiO
h
i
j
Cell counts×10^6 / mm^2
***
NiO/A. succinogenes
NiO@PAA@NHS/Au@A. succinogenes

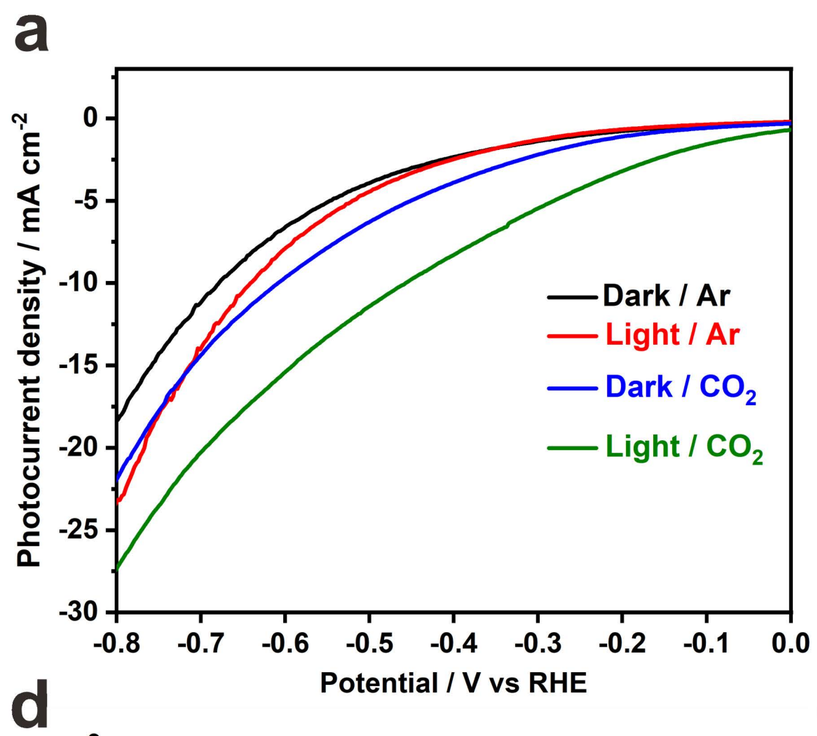
a
Photocurrent density / mA cm-2
Potential / V vs RHE
Dark / Ar
Light / Ar
Dark / CO2
Light / CO2

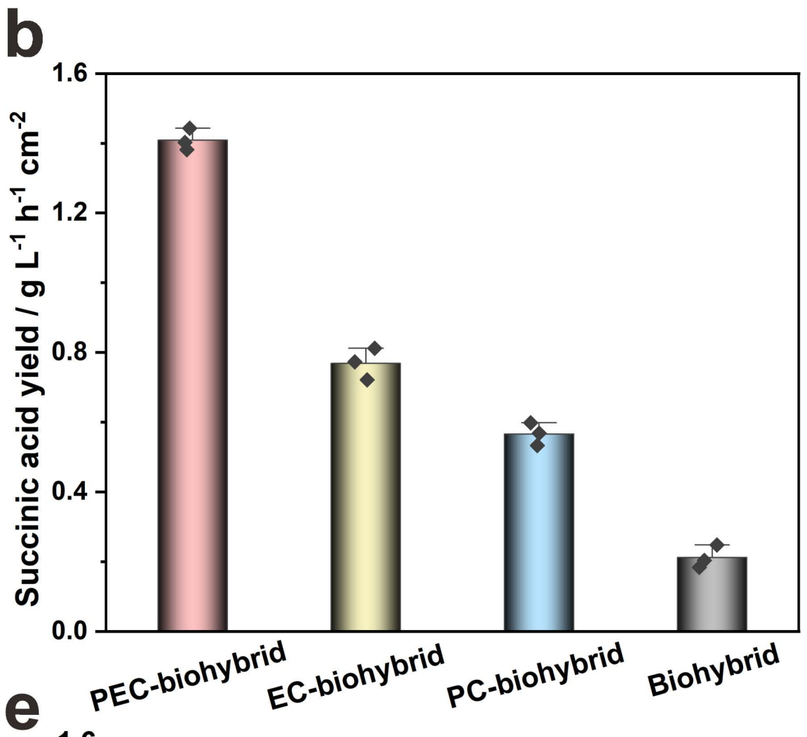
b
Succinic acid yield / g L-1 h-1 cm-2
PEC-biohybrid
EC-biohybrid
PC-biohybrid
Biohybrid

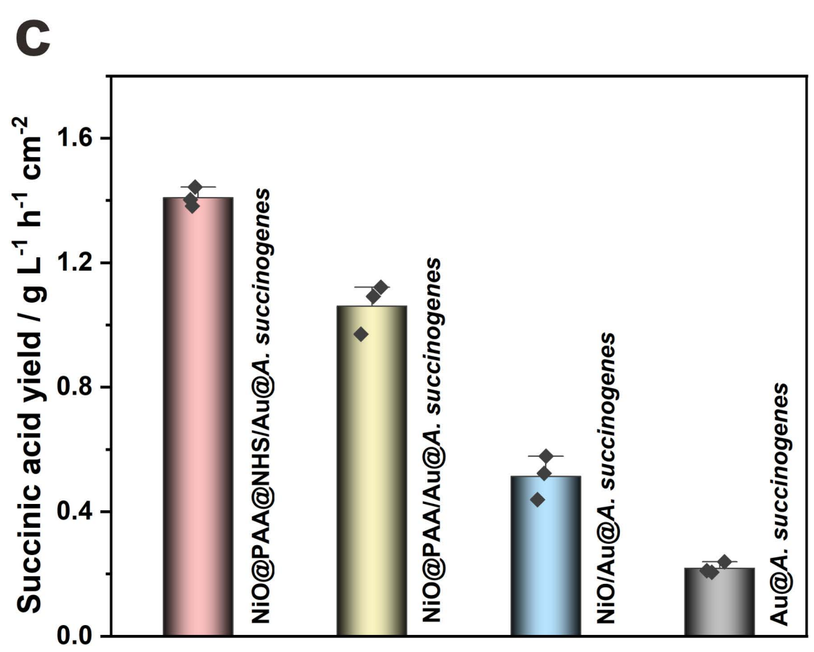
c
Succinic acid yield / g L-1 h-1 cm-2
NiO@PAA@NHS/Au@A. succinogenes
NiO@PAA/Au@A. succinogenes
NiO/Au@A. succinogenes
Au@A. succinogenes

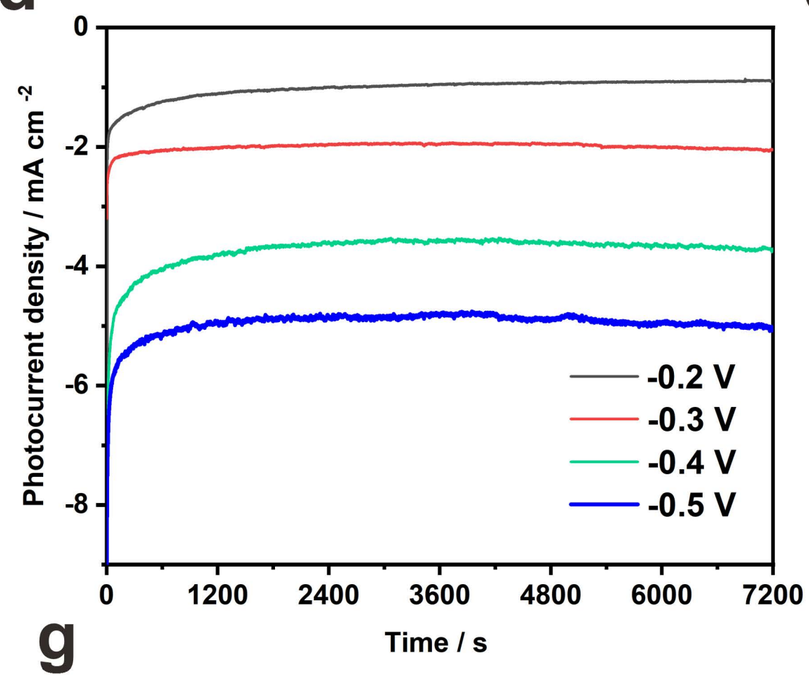
d
Photocurrent density / mA cm-2
Time / s
-0.2 V
-0.3 V
-0.4 V
-0.5 V

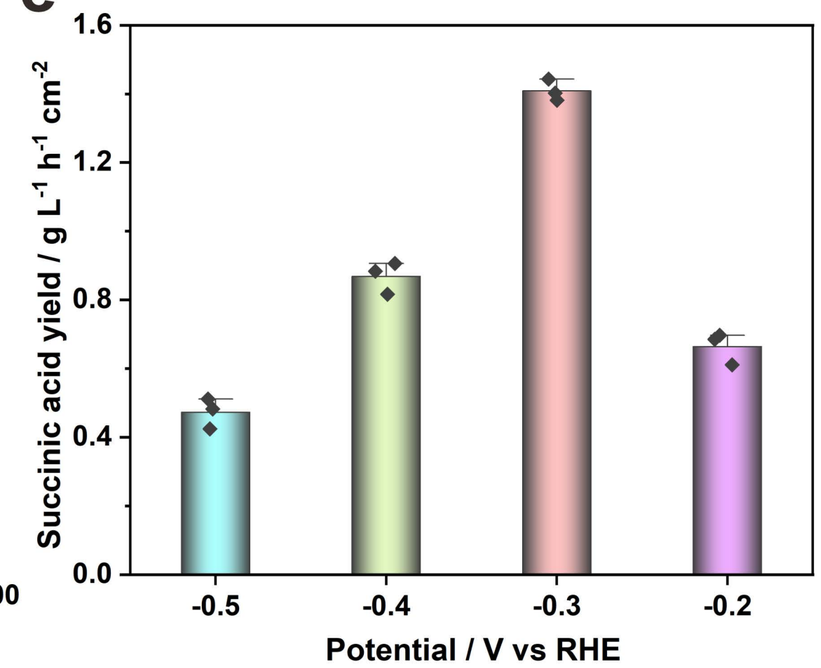
e
Succinic acid yield / g L-1 h-1 cm-2
Potential / V vs RHE

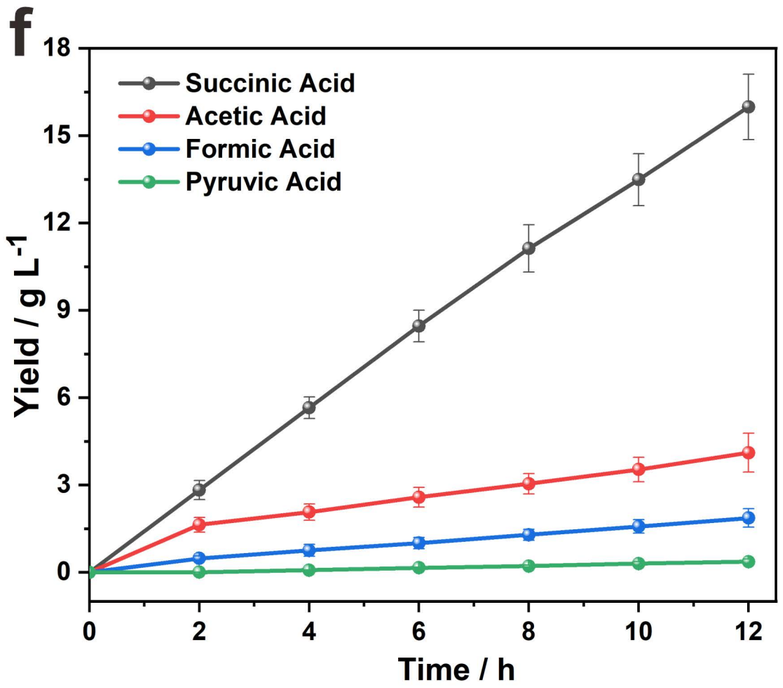
f
Succinic Acid
Acetic Acid
Formic Acid
Pyruvic Acid
Yield / g L-1
Time / h

g
Succinic acid yeild / g L-1 cm-2
Light
Dark
Time / h

h
Succinic acid yeild rate / g L-1 h-1
This work
G.sulfurreducens/carbon dots
A. succinogenes/carbon-felt
Y. lipolytica PGC01003
E.coli BW16
C.amalonaticus/graphite
B. succiniciproducens
E. coli NZN111
S. cerevisiae
A. succinogenes CCTCC
A. succinogenes CGMCC
E. coli AFP111
A. succinogenes FZ53
PC
PC
EC
MF
MF
EC
MF
MF
MF
MF
MF
MF
MF

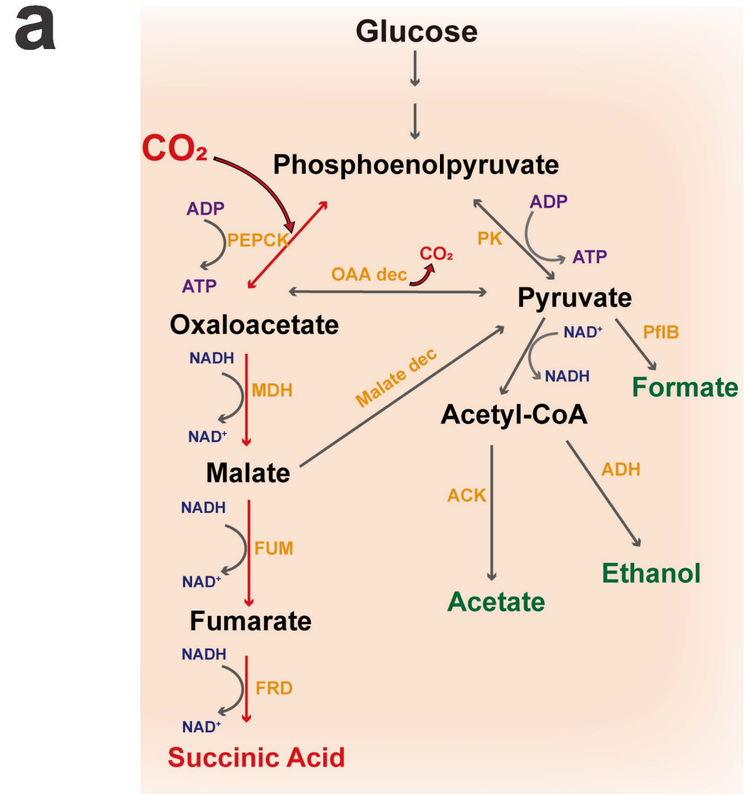
a
Glucose
CO2
Phosphoenolpyruvate
ADP
PEPCK
ATP
OAA dec
CO2
ADP
PK
ATP
Pyruvate
Oxaloacetate
NADH
MDH
NAD+
Malate dec
NAD+
NADH
PflB
Formate
Acetyl-CoA
Malate
ACK
ADH
NADH
FUM
NAD+
Ethanol
Acetate
Fumarate
NADH
FRD
NAD+
Succinic Acid

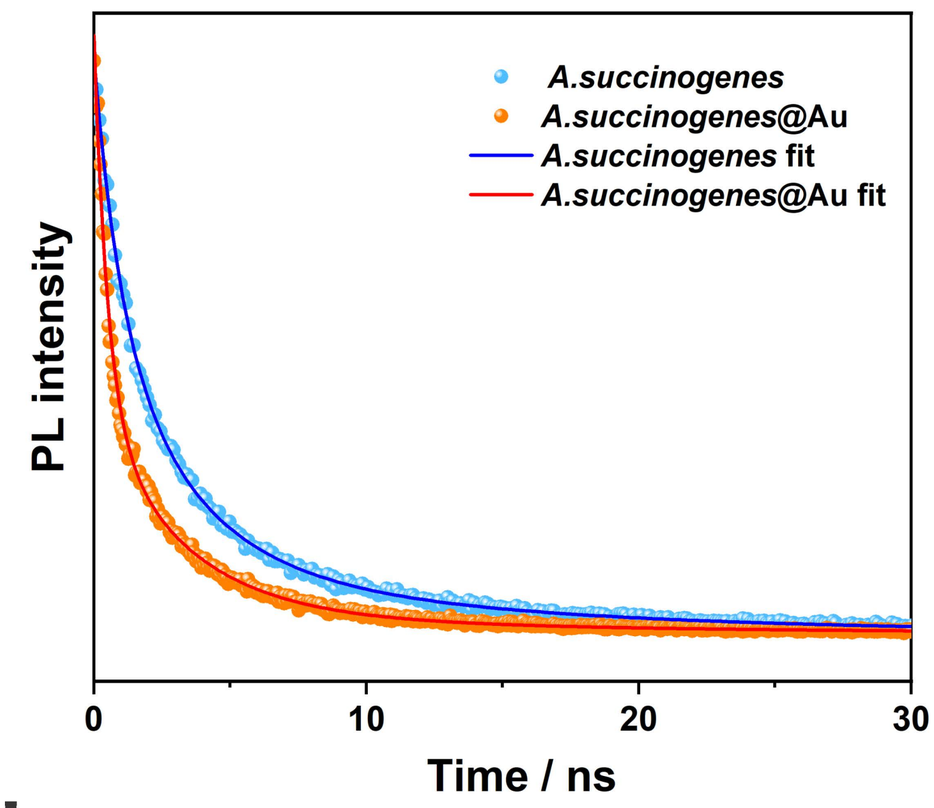
b
A.succinogenes
A.succinogenes@Au
A.succinogenes fit
A.succinogenes@Au fit
PL intensity
0
10
20
30
Time / ns

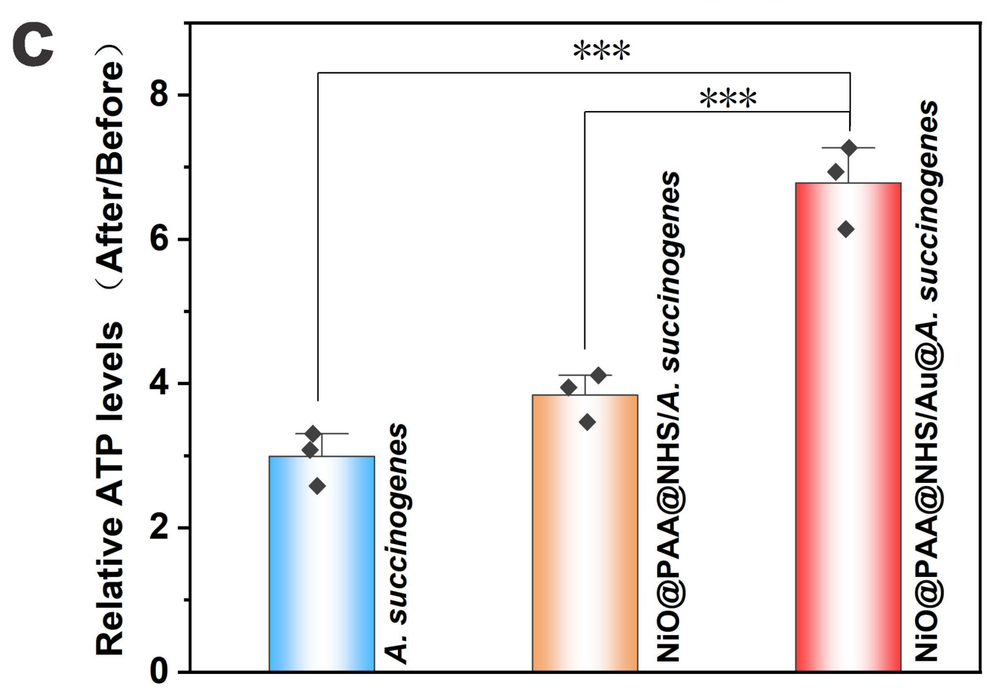
c
***
***
Relative ATP levels（After/Before）
0
2
4
6
8
A. succinogenes
NiO@PAA@NHS/A. succinogenes
NiO@PAA@NHS/Au@A. succinogenes

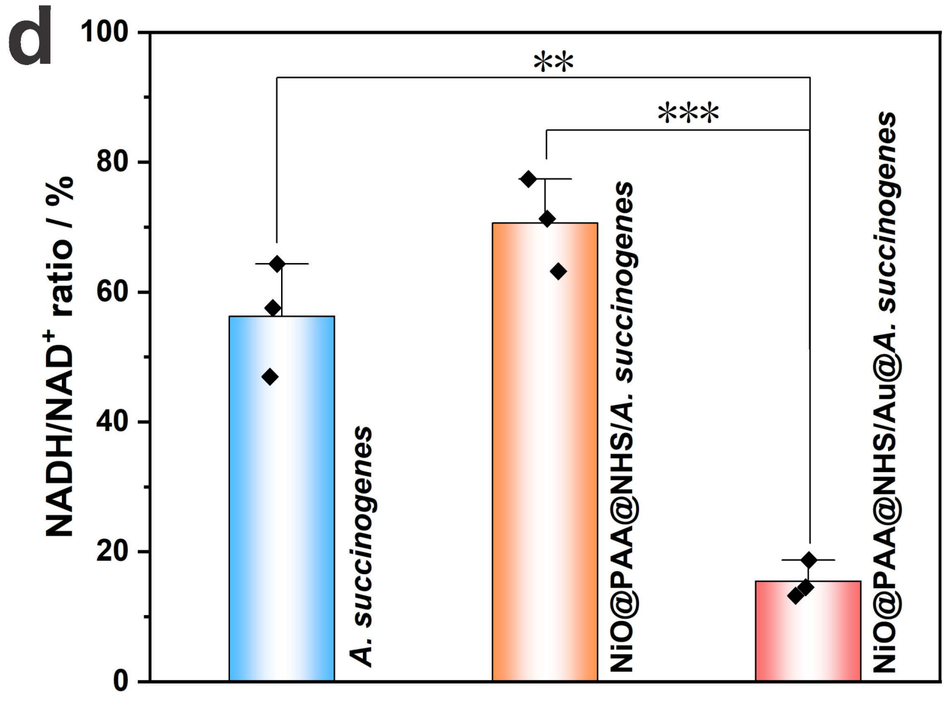
d
**
***
NADH/NAD+ ratio / %
0
20
40
60
80
100
A. succinogenes
NiO@PAA@NHS/A. succinogenes
NiO@PAA@NHS/Au@A. succinogenes

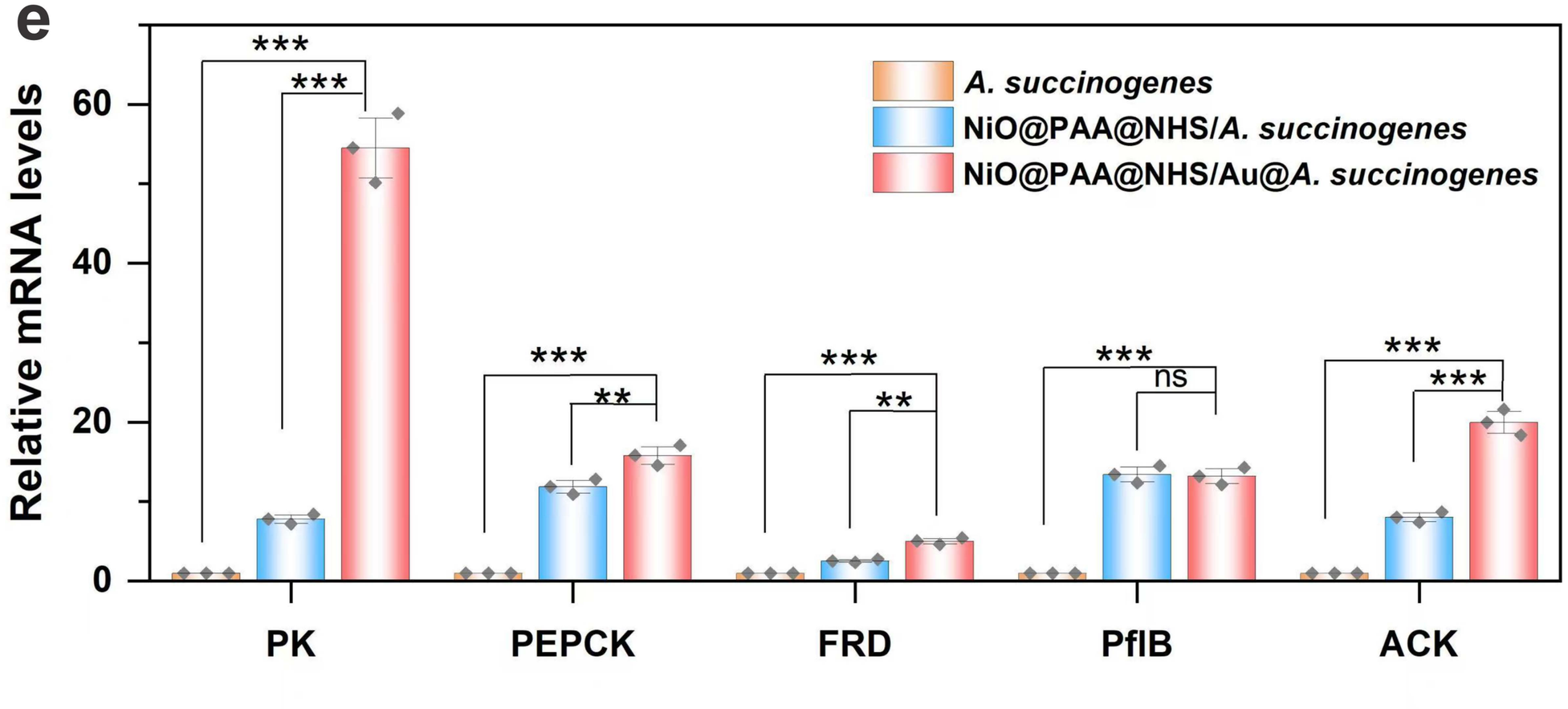
e
Relative mRNA levels
0
20
40
60
A. succinogenes
NiO@PAA@NHS/A. succinogenes
NiO@PAA@NHS/Au@A. succinogenes
***
***
***
**
***
**
***
ns
***
***
PK
PEPCK
FRD
PflB
ACK